Selected techniques in diamond anvil cell crystallography: centring samples using X-ray transmission and rocking powder samples to improve X-ray diffraction image quality

Jesse S. Smith* and Serge Desgreniers

Laboratoire de physique des solides denses, University of Ottawa, Ottawa, Ontario, Canada K1N 6N5. E-mail: jsmit068@uottawa.ca

The distinct X-ray transmission profile obtained by scanning a sample in a diamond anvil cell across a collimated X-ray beam is used to monitor sample displacement brought about by rotation. This measured displacement can in turn be used to calculate, and subsequently correct, the sample position with respect to a centre of rotation. This centring method differs from others also based on transmission in that it does not require a 180° sample rotation, nor does it require prior positioning of the rotation axis in the path of the X-ray beam. After a full description of the method, an example is presented together with an extended record of use to evaluate the method in a practical setting. The practice and benefits of rocking polycrystalline samples during X-ray exposure have also been quantitatively examined. Changing the orientation of the sample grains with respect to the incident beam yields the expected result of a more homogeneous intensity distribution along Debye rings. Interestingly, by limiting the amount of time large grains assume a particular orientation, rocking brings about the added effect of significantly reducing detector saturation. Sample rocking yields more reliable relative intensities, a more appropriate line shape and narrower line width. Data are presented for a calibration standard at ambient pressure as well as a research sample at high pressure.

Keywords: centring; diamond anvil cell; high pressure; X-ray diffraction; X-ray diffraction methods; rocking.

1. Introduction

The diamond anvil cell (DAC) is a remarkable tool in that it combines conceptual simplicity in design and operation with exceptional results in attainable pressures and practicable methods. In the context of high-pressure crystallography, however, these virtues are accompanied by a number of technical challenges. Difficulties such as X-ray absorption by the diamond anvils, the limited scattering range imposed by the anvils' supporting structure, and minute sample volumes are mitigated by the use of synchrotron radiation, as the small source size, near-parallel beam and high particle storage-ring energy of a typical synchrotron source allow a tremendous flux of high-energy X-rays to be delivered to microscopic samples. The threefold advantage is that the anvils become almost transparent, the accessible range of reciprocal space is significantly increased for a fixed DAC aperture, and intense scattering can be recorded from minute samples in a matter of minutes.

The use of synchrotron radiation, however, does not overcome all of the obstacles presented by the DAC. The severely limited sample volume necessary to reach high-pressure conditions puts finite limits on the number of diffracting crystallites in polycrystalline samples. Furthermore, polycrystalline samples are often 'prepared' *in situ* (*e.g.* a pressure-induced structural phase transition), under non-hydrostatic pressure conditions. In short, they are frequently far from ideal powders. These difficulties can even be exacerbated by the use of synchrotron radiation, as the highly parallel beam further limits the number of crystallographic planes which satisfy the Bragg condition (as compared with beams with moderate divergence, typically encountered in laboratory X-ray sources). It is therefore imperative that the user employ a number of experimental techniques to obtain data of the highest quality and, hence, structural parameters of the highest accuracy. The present work constitutes a detailed study of two of these experimental techniques: reproducible sample positioning at the centre of rotation in the experimental configuration, and rocking polycrystalline samples to improve the quality of powder X-ray diffraction images.

Following a brief description of the synchrotron radiation source, experimental configuration and analysis software

research papers

common to the study as a whole, separate sections, each including a more detailed overview, experimental procedure, results and summary, are dedicated to the respective selected techniques. Although these techniques are presented in the context of DAC crystallography, their generic nature is such that they could likely be beneficially applied or adapted to a broad range of experimental configurations in the field of X-ray scattering.

2. Source and software

All data presented in this work were collected at the Hard X-ray Microanalysis (HXMA) beamline at the Canadian Light Source. HXMA is a multipurpose beamline providing users with EXAFS, microprobe, imaging and diffraction capabilities. The source is a 63-pole superconducting wiggler with a critical energy of approximately 10 keV. Wavelength is selected using either the Si(111) or (220) crystals of a fixed-exit double-crystal monochromator. Optional beamline optics include a plane parabolic mirror for collimating the continuous spectrum in the horizontal plane, as well as a toroidal mirror for focusing the monochromatic beam in both the horizontal and vertical planes. The final beam size is defined by square-aperture collimators [similar in design to those described by Ruoff *et al.* (1993)] ranging from 15×15 μm to 45×45 μm. Specific details regarding incident X-ray energy, beamline configuration and collimator size are provided in the respective descriptions of the centring and rocking studies. All X-ray diffraction images were obtained using transmission geometry, with scattering recorded on a Marresearch mar345 imaging-plate detector (located approximately 270 mm from the sample), and were scanned at 100 μm pixel resolution.

FIT2D (Hammersley *et al.*, 1996) was used extensively for data analysis and image processing. For the centring study, it was used to determine the sample-to-detector distance, based on powder X-ray diffraction images from calibration standards. For the rocking study, it was used to convert diffraction images into conventional diffraction patterns of intensity *versus* 2θ, and to produce the figures containing portions of powder diffraction images. With regard to the latter, it is important to note for each figure containing sets of images that each image is presented with the same intensity scaling. Furthermore, it is important to note that, for all images, saturated pixels were masked prior to any data analysis. *FullProf* (Rodriguez-Carvajal, 2006) was used to carry out Rietveld refinements on the LaB_6 diffraction patterns for the rocking study. Refined parameters included the background, scale factor, lattice constant, asymmetric pseudo-Voigt peak profile, B (overall) and fractional x-coordinate of boron.

3. Centring

3.1. Overview

Accurate reproducible sample positioning is a prerequisite for practically any X-ray diffraction experiment. A number of different positioning methods have been devised, depending on factors such as the source, geometry or specific type of measurement to be performed. When carrying out diffraction using a DAC in transmission geometry with an area detector, the sample-to-detector distance, D, is a crucial experimental parameter as it is required to convert the spatial position of observed Bragg spots or the radial position of observed Debye rings into the appropriate scattering variable. A fractional uncertainty in D will result in approximately the same fractional uncertainty in d-spacings. Typically, D is determined by recording a powder X-ray diffraction image of a calibration standard with well known lattice constants (*e.g.* Si, LaB_6 or CeO_2) at ambient conditions. The radial position of the recorded Debye rings, together with monochromatic radiation of known wavelength (independently determined, for example, by scanning an absorption edge of an elemental calibration foil), can be used to accurately determine D. The goal, of course, is to subsequently place research samples at the same position as the standard, such that all share a unique and well defined D. Making this unique position a centre of rotation is a natural choice, both for conventional multi-circle diffractometers as well as for custom multi-stage goniometers often employed for high-pressure studies at synchrotron radiation facilities.

Traditionally, optical methods are used for positioning a sample at the centre of rotation. The sample is rotated while observed through a microscope, and any initial displacement of the sample from the centre of rotation results in both lateral and telescopic motion of the sample upon rotation. Corrections are made to the sample position to minimize the observed motion upon rotation. Optical methods are not practical when using DACs because the optical access to the sample is severely limited by the anvils' supporting structure, and furthermore the high refractive index of diamonds introduces additional challenges, particularly as the optical path length increases upon rotation. Alternatively, Hamilton (1974) showed that the sample position with respect to the centre of rotation could be determined from the observed angles of pairs of single-crystal reflections. An adaptation of this method was first applied to DACs by King & Finger (1979), and further generalized by Dera & Katrusiak (1999). The obvious limitation of a method based on single-crystal reflection pairs is that the problem of positioning polycrystalline samples is not resolved. Furthermore, these methods are based on traditional geometries which include a point detector situated at a constant distance from the centre of rotation.
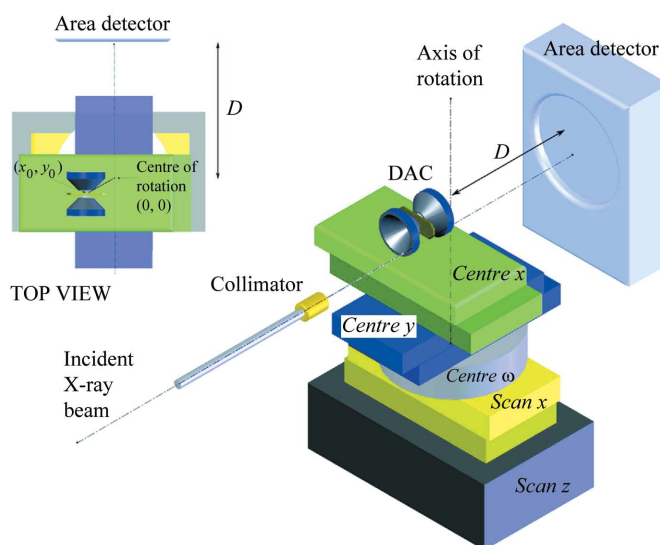
The method of centring presented in this work is related to the optical method in that it relies upon the observed sample displacement upon rotation; however, it does not rely on the eye to monitor this displacement but rather on the characteristic transmission profile obtained by scanning a gasketed DAC sample across a spatially well defined X-ray beam. Specifically, the sample position with respect to the fixed X-ray beam is measured at three separate sample rotation angles, and the corresponding sample displacement is used to calculate the position of the sample with respect to the centre of rotation. Similar methods for sample centring based on X-ray

transmission through the DAC have been described by Budzianowski & Katrusiak (2004) and Kunz *et al.* (2005); however, in both cases centring is carried out in a step-wise fashion: the sample must first be centred along one (or both) of the axes normal to the beam, after which the sample is centred along the axis parallel to the beam. To accomplish this first step, Bunzianowski & Katrusiak prescribe a 180° sample rotation, whereas Kunz *et al.* do not explicitly specify how the first step is carried out. The method presented here differs in that the sample position with respect to the centre of rotation can be determined in two dimensions, along one of the axes normal to the beam as well as along the axis parallel to the beam, simultaneously. Furthermore, the method does not require a 180° sample rotation. This last point is particularly important as it is often either not feasible or not possible to rotate the sample in this manner owing to ancillary equipment such as a cryostat, furnace or pneumatic DAC membrane assembly, or owing to the close proximity of peripheral beam-conditioning equipment such as a collimator, 'clean-up' aperture or radiation shielding. One final point worth iterating is that the method works equally well for powder and single-crystal samples inasmuch as the characteristic profile used to define the sample position is due to the gasket rather than the sample.

After considering some preliminary details, a simplified version of the centring technique, suitable for most DAC applications, is presented. This version is then generalized for use in a wider range of applications. An example of the centring technique, together with an extended record of its use, over several days of experiments employing several beamline configurations, is presented to emphasize some practical considerations as well as possible limitations.

3.2. Coordinates and nomenclature

Fig. 1 shows a schematic diagram of the experimental configuration, together with a definition of the coordinate system. The positive *y*-axis runs parallel to the beam, the positive *z*- and *x*-axes make up the vertical and horizontal axes, respectively, of the plane normal to the beam, with the former pointing upward and the latter completing the right-handed coordinate system. The rotation axis ω is collinear with the *z*-axis, with positive rotation in the counter-clockwise direction when viewed from above. Starting at the base of the assembly, the *Scan z* and *Scan x* stages are employed for scanning the sample in the plane normal to the X-ray beam, *Centre ω* allows for the sample rotation necessary to carry out the centring process, and *Centre x* and *Centre y* are used to place the sample at the centre of rotation. All stages are motorized, with optical encoder resolution equal to or better than 0.1 µm, and with a unidirectional repeatability of just over 1 µm. It should be mentioned that, for the purposes of centring as described in the present work, it is compulsory to have *x* motion below the rotation stage for scanning the sample in the fixed reference frame of the hutch, and it is necessary to have *x–y* motion above the rotation stage to position samples at the centre of rotation. The particular
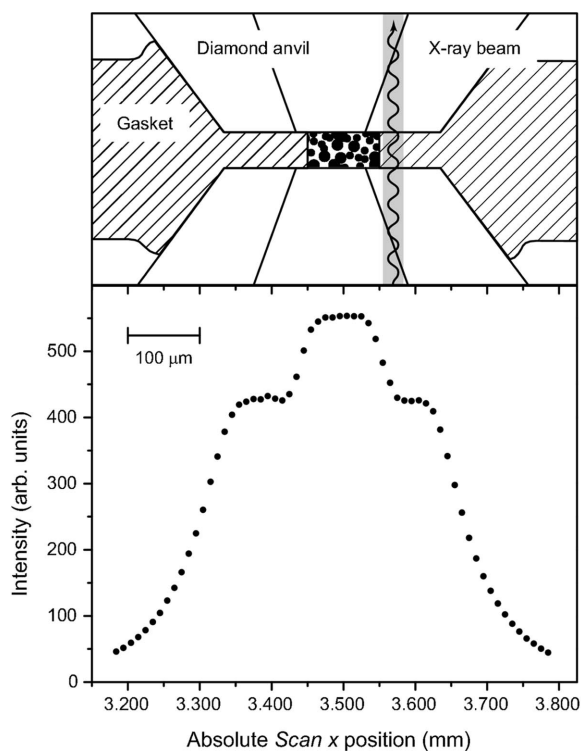

Figure 1
Schematic diagram of the experimental configuration and coordinate system. Motorized stage names are in italics. The top view is shown for the case of *Centre ω* at ω_0 (translation of the sample along *y* results in zero displacement along *x*) and illustrates an initial sample displacement (x_0, y_0) with respect to the centre of rotation.

location of *z* motion is a matter of choice in the current context.

3.3. Transmission profile and sample position

Fig. 2 shows a typical example of the transmission profile obtained by scanning the sample across the X-ray beam. The monochromatic focused X-ray beam was collimated using a square 30 µm aperture. (Note that for the purposes of this work it is assumed that the maximum beam dimensions do not exceed the minimum diameter of the sample chamber; in practice this is almost always the case as diffraction from the gasket material surrounding the sample introduces difficulty during data analysis.) The DAC had diamond anvils with 300 µm culets. The indented stainless steel gasket (T301, full-hard) was approximately 50 µm thick, with a sample chamber 100 µm in diameter. A schematic diagram of the anvils–gasket–sample region is shown in Fig. 2 above the plot. If one imagines the X-ray beam (shown to proper scale in the diagram) moving across the sample, with transmission intensity being recorded at discrete 10 µm intervals, the characteristic features of the transmission profile, two shoulder plateaus and one peak plateau, are readily obtained.

Placing the sample in the path of the X-ray beam is straightforward with such a transmission profile. However, for the purposes of centring it is important to define a unique sample position with the greatest possible accuracy. Furthermore, this unique position must still be identifiable in scans taken with the DAC at some angle with respect to the beam. Because of the plateau nature of the profile shown in Fig. 2, the position of maximum intensity can be ambiguous and is therefore rarely reliable for such purposes, so instead the position coordinate of the centroid (commonly referred to as the centre of mass) is used to define the sample position. This

research papers

Figure 2
Typical example of the X-ray transmission profile intensity as a function of the scanning stage position. Above the plot is a schematic diagram (to scale) detailing the diamond anvils, gasket and sample configuration giving rise to such a characteristic profile. Note that the shaded region about the X-ray beam is scaled to correspond to 30 μm, the collimated width of the incident X-ray beam.

does not entirely solve the problem of defining an unambiguous sample position, as factors such as gasket material, gasket deformation at high pressure, sample chamber displacement from the centre of the gasket indentation, and choice of scan parameters can all contribute to deviations from the ideal shape and/or symmetry (or similarly, a consistent shape and/or symmetry) of the characteristic profile. These practical difficulties will be briefly addressed in the analysis and discussion.

3.3.1. Mathematical description. Prior to carrying out the centring routine, *Scan z* and *Scan x* are used to scan the sample in the plane normal to the beam and subsequently position the sample in the path of the beam. The centring routine requires the sample position, in *Scan x* space, to be determined at three unique angles. First, the position is determined at $\omega_0 = 0°$. (This angle is defined as the angle at which the sample can be translated along the beam and undergo no translation in the x direction.) The position of the sample is then determined for $\Delta\omega = \omega_+$ and ω_- (with an approximate range of 5°–35° for possible $\Delta\omega$ values). It is important to note that, for the description of the method as applied to DACs, $|\omega_-| = \omega_+$ is a requirement inasmuch as the method takes advantage of the even and odd properties of the cosine and sine functions, respectively (this requirement will be subsequently lifted for the generalized method). The sample displacement in *Scan x* space brought about by rotation is then used to calculate the sample position with respect to the centre of rotation.

Turning to a more complete mathematical description, when the sample is first placed on the positioning assembly, its position with respect to the centre of rotation (see Fig. 1, top view) can be expressed by a vector,

$$\mathbf{P}_0 = x_0 \hat{\mathbf{i}} + y_0 \hat{\mathbf{j}}. \tag{1}$$

Upon rotating the sample assembly through an angle ω, the new position of the vector in the fixed coordinate system of the experimental hutch is found by applying a coordinate transformation for pure rotation,

$$\begin{array}{c} x_\omega \\ y_\omega \end{array} = \begin{bmatrix} \cos\omega & -\sin\omega \\ \sin\omega & \cos\omega \end{bmatrix} \begin{array}{c} x_0 \\ y_0 \end{array}, \tag{2}$$

such that

$$\mathbf{P}_+ = (x_0 \cos\omega_+ - y_0 \sin\omega_+)\hat{\mathbf{i}} + (x_0 \sin\omega_+ + y_0 \cos\omega_+)\hat{\mathbf{j}} \tag{3}$$

and

$$\mathbf{P}_- = (x_0 \cos\omega_+ + y_0 \sin\omega_+)\hat{\mathbf{i}} + (-x_0 \sin\omega_+ + y_0 \cos\omega_+)\hat{\mathbf{j}}. \tag{4}$$

It is important to note that in (4) the even and odd properties of the cosine and sine functions, respectively, have been exploited such that $\mathbf{P}_-$ is written in terms of ω_+ (all subsequent equations will be written in terms of the positive angle, allowing the subscript on ω to be dropped). The experimentalist is privy only to the projection of the sample displacement onto *Scan x* space, which depends on the initial displacement (x_0, y_0) as well as the choice of ω,

$$(\mathbf{P}_+ - \mathbf{P}_0) \cdot \hat{\mathbf{i}} \rightarrow \delta Sx_+ = x_0(\cos\omega - 1) - y_0 \sin\omega \tag{5}$$

and

$$(\mathbf{P}_- - \mathbf{P}_0) \cdot \hat{\mathbf{i}} \rightarrow \delta Sx_- = x_0(\cos\omega - 1) + y_0 \sin\omega. \tag{6}$$

At this point it is necessary to introduce a small correction to the description. Because the beam remains stationary, each time the sample is displaced it is actually the entire coordinate system that must be translated to bring the sample back into line with the beam. To account for this, one simply needs to distribute a negative sign through (5) and (6), $-\delta Sx \rightarrow \Delta Sx$ yielding,

$$\Delta Sx_+ = x_0(1 - \cos\omega) + y_0 \sin\omega \tag{7}$$

and

$$\Delta Sx_- = x_0(1 - \cos\omega) - y_0 \sin\omega. \tag{8}$$

Solving this simple system yields the final result,

$$x_0 = \frac{\Delta Sx_+ + \Delta Sx_-}{2(1 - \cos\omega)} \tag{9}$$

and

$$y_0 = \frac{\Delta Sx_+ - \Delta Sx_-}{2 \sin\omega}. \tag{10}$$

Relative motions of *Centre x* and *Centre y* by $-x_0$ and $-y_0$, respectively, will place the sample at the centre of rotation. Subsequent relative motion of *Scan x* by x_0 is then required to bring the sample back into the beam's path.

3.3.2. Generalized method. In the majority of X-ray scattering applications associated with DACs, the X-ray beam passes straight through the load axis. The accessible angular range about this load axis is typically symmetric and, furthermore, it is often quite limited owing to the diamond anvil supports. With this in mind, the specific method of centring presented above is well suited for DACs. However, there is no *a priori* reason for requiring that ω_0 be used, or for requiring the other two angles to be symmetric about ω_0, and therefore the method can be generalized to any three angles. Notably, the general method is not limited to atypical DAC applications; it could be employed in any experimental configuration for which the experimentalist can monitor the transverse displacement of a unique transmission feature upon rotation. In the general case, the sample position is measured at three angles α, ω and γ. Here no restrictions are made regarding the signs or values of the angles, except that they are known with respect to ω_0. Following the same procedure described above, one obtains the general form for the corrections,

$$x_0 = \frac{(\sin\gamma - \sin\alpha)\Delta Sx_\omega - (\sin\omega - \sin\alpha)\Delta Sx_\gamma}{(\cos\alpha - \cos\omega)(\sin\gamma - \sin\alpha) - (\sin\omega - \sin\alpha)(\cos\alpha - \cos\gamma)} \tag{11}$$

and

$$y_0 = \frac{(\cos\alpha - \cos\omega)\Delta Sx_\gamma - (\cos\alpha - \cos\gamma)\Delta Sx_\omega}{(\cos\alpha - \cos\omega)(\sin\gamma - \sin\alpha) - (\sin\omega - \sin\alpha)(\cos\alpha - \cos\gamma)}. \tag{12}$$

If $\alpha \to \omega_0 = 0°$, one obtains

$$x_0 = \frac{(\sin\gamma)\Delta Sx_\omega - (\sin\omega)\Delta Sx_\gamma}{(1 - \cos\omega)(\sin\gamma) - (\sin\omega)(1 - \cos\gamma)} \tag{13}$$

and

$$y_0 = \frac{(1 - \cos\omega)\Delta Sx_\gamma - (1 - \cos\gamma)\Delta Sx_\omega}{(1 - \cos\omega)(\sin\gamma) - (\sin\omega)(1 - \cos\gamma)}. \tag{14}$$

Finally, if $\gamma \to -\omega$, and the even/odd properties of the cosine/sine functions are used to write everything in terms of ω, one obtains equations (9) and (10).

3.4. Example

For the example presented here, as well as for the extended record of use of the centring method presented thereafter, the simplified centring method, with ω_0 and symmetric angles about ω_0, was used. A simple macro was employed, for which the user is required to input three parameters: the scan width (more specifically, the initial and final positions of the scan relative to the current *Scan x* position), the discrete step size and $\Delta\omega$. The same scan width and step size are used for each of the three ω angles. After the three scans are completed, the macro calculates the position coordinate of the centroid for each scan, and subsequently calculates the sample position with respect to the centre of rotation.

To facilitate the establishment of an accurate unique sample-to-detector distance D for all samples, calibration samples are mounted in DAC gaskets so as to mimic the centring process as it is carried out on regular research samples. The calibration samples are prepared by first indenting and drilling a stainless steel gasket with roughly the same dimensions as described for Fig. 2. After replacing the gasket in the DAC, the calibration sample is loaded into the sample chamber and gently packed using the opposing anvils. The gasket is removed from the DAC, covered with thin polyimide tape for protection, and permanently fixed in a custom mount. The calibration and DAC mounts are designed such that when a calibration sample is placed atop the sample goniometer it rests at approximately the same position as the mounted DAC samples. This is done to minimize long travel with any of the stages when switching between samples, thus minimizing errors introduced by slight deviations from orthogonality among stages in the sample assembly.

Fig. 3 shows an example of iterative use of the centring method. For each trio of scans, the relative scan endpoints were −300 to 300 μm, with a step size of 10 μm. $\Delta\omega$, the measured ΔSx displacements, and the calculated sample positions with respect to the centre of rotation (*i.e.* the x- and y-components of P_0) are presented in Table 1. The first iteration is represented by the top trio of scans. Despite the modest value of ω, the sample displacement owing to rotation, approximately ±14 μm for ω_+ and ω_-, respectively, is clearly noticeable. After making the calculated corrections, the centring process was repeated, only now $\Delta\omega$ was increased to ±10°. The resulting trio of scans in the middle of Fig. 3 shows a marked improvement; however, it is clear that the sample is still displaced slightly upon rotation. Again the calculated corrections were applied and the routine was executed a third and final time, with the resulting trio of scans shown at the bottom of Fig. 3.
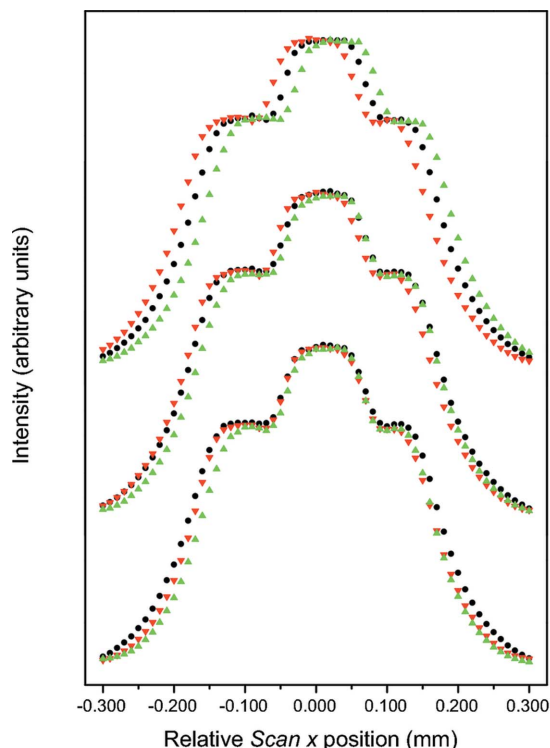
Considering the iterative progression of the calculated corrections in Table 1, it is reasonable to estimate that, after applying the calculated corrections from the third iteration, a small positioning error of the sample centre with respect to the centre of rotation still persists, perhaps a little more than 10 μm along x and a little less than 10 μm along y. However, given the dimensions of the sample, this estimate puts the centre of rotation well within the sample volume. Considering the iterative progression of the sample displacement brought about by rotation, it is reasonable to conclude that rotation of the sample by ±10° (*i.e.* rocking the sample) during image capture would result in a sample displacement of not more than ±2.5 μm normal to the beam. Based on the estimated positioning error, the sample displacement along the beam would be slightly larger (*e.g.* less than ±5 μm for a 25 μm positioning error along x).

The final result presented in the description of the method, equations (9) and (10), is exact provided a unique feature can be identified and used to define the sample position for all pertinent values of ω. Unfortunately this is rarely the case, as demonstrated by the iterations required in this example. It is worth exploring some of the related factors that cause uncertainty in defining a unique sample position. This will not only provide some insight into the practical limitations of the

Table 1
Choice of $\Delta\omega$, the resulting projections onto *Scan x* space of the sample position owing to rotation, and the calculated correction from equations (9) and (10), for each iteration of the centring process for the example shown in Fig. 3.

Iteration	$\Delta\omega$ (°)	ΔSx_+ (µm)	ΔSx_- (µm)	x_0 (µm)	y_0 (µm)
First	5	14.1	−14.3	−24	163
Second	10	3.5	−7.6	−135	32
Third	10	2.7	−1.2	50	11

Figure 4
Calculated correction per unit numerator value of equation (9) along x (squares) and equation (10) along y (circles), as a function of $\Delta\omega$. The inset details the extreme correction along x for small angles. The dotted line at 10° is to draw attention to the angle used in the second and third iterations of the example.
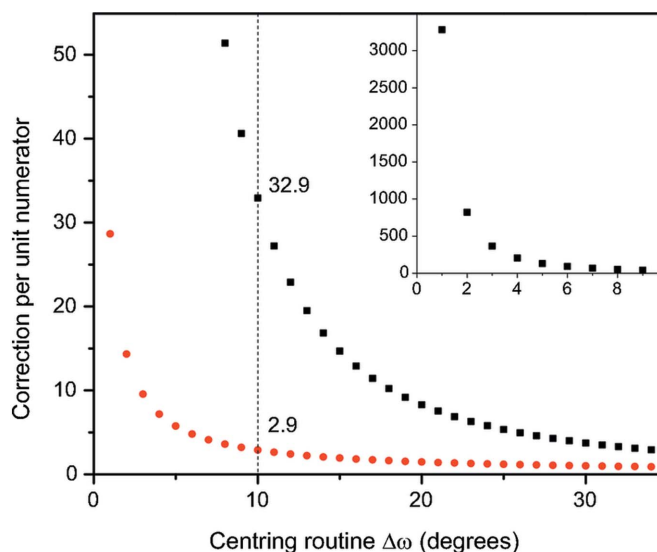

Figure 3
Three iterations, in order from top to bottom, of the centring process. In each trio of scans the circles, triangles and inverted triangles correspond to $\omega = \omega_0$, ω_+ and ω_-, respectively. With each iteration the displacement of the sample chamber portion of the profile is progressively minimized.

method, but will also lead to suggestions for utilizing the method to obtain the best possible result.

3.5. Discussion

The problem of identifying unique profile features for an arbitrary rotation angle is due primarily to a lack of uniformity in the characteristic transmission profile. Upon rotating the sample, the width of the features in the transmission profile are compressed by a factor of $\cos(\omega)$. For small ω, the corresponding effect is small, but for larger values of ω the difference can be substantial. Atypical features, caused for example by a deformed or unstable gasket at high pressure, or asymmetric features, for example a sample chamber not well centred in the gasket indentation, can exacerbate this problem. However, a careful choice of scan parameters can greatly mitigate these difficulties. In the example presented above, the entire profile was included in the scan width (the

narrower transmission profiles for $\Delta\omega = \pm 10°$ are clearly visible in the tails of the bottom trio of Fig. 3). This generous scan width yielded satisfactory results; however, for the most demanding applications, the scan width can be chosen to include only the sample chamber and a few data points of each shoulder plateau to minimize uncertainty caused by asymmetric or atypical transmission profiles.

The choice of ω is particularly crucial. To appreciate this more fully, Fig. 4 shows the calculated correction obtained from equations (9) and (10), per unit numerator value, as a function of $\Delta\omega$. For example, if one executes the centring routine with $\Delta\omega = \pm 10°$ and finds the sum $\Delta Sx_+ + \Delta Sx_- = 1$ µm, the magnitude of the calculated sample displacement x_0 would be 32.9 µm. Conversely, if one finds the difference $\Delta Sx_+ - \Delta Sx_- = 1$ µm, the magnitude of the calculated sample displacement y_0 would be just 2.9 µm. To reiterate, errors in positioning are the result of not accurately identifying the same unique feature for all ω. For small ω the distortion of the profile owing to rotation, and therefore the detrimental effect on the consistency and symmetry of the profile, is minimized, but at the same time small errors in positioning are magnified by the relatively large calculated correction, particularly for x_0. For large ω the magnitudes of the calculated corrections are much smaller, but at the same time the detrimental effect of rotation on the profile consistency can be substantial. For all values (and particularly small values) of ω, the method is more precise parallel to the beam than it is normal to the beam. One notable exception is the case of a 180° rotation. The method presented in this work does not require such a rotation, but it is important to note that the method nevertheless works for such a rotation and, when possible, this is still the ideal choice to position the sample along the axes normal to the beam. However, this gives no information about the displacement y_0,

Table 2
A record of several calibration images taken over several days of X-ray diffraction experiments.

An asterisk (*) indicates that there is no relation to the centre stage positions above owing to a change in the calibration mounts. A dagger (†) indicates that the sample was not disturbed between images. Notably, a change in beamline configuration and/or calibration sample brings about the most abrupt changes in D.

Standard	Day	Time	Configuration	Centre y (mm)	D (mm)
LaB$_6$	1	00:45	1	3.913	271.756
LaB$_6$	1	13:30	1	3.920	271.794
LaB$_6$	2	04:00	2	3.925	271.837
LaB$_6$	2	13:30	2	3.927	271.853
LaB$_6$	2	16:00	2	3.927	271.847
LaB$_6$	2	17:30	2	3.929	271.840
LaB$_6$	2	23:30	2	3.933	271.859
Si	3	0:00	2	4.015*	271.721
Si	3	14:00	2	4.020	271.715
LaB$_6$	4	5:30	3	3.855*	271.992
LaB$_6$	4	5:40	3	3.855†	272.001
LaB$_6$	6	4:00	4	3.889	271.854
LaB$_6$	6	4:30	4	3.889†	271.875

Table 3
Parameters detailing the four beamline configurations employed during the record of use.

Configuration	Energy (keV)	Mono (hkl)	Focusing optics?	Beam size (µm)
1	24.030	(111)	Yes	15 × 15
2	24.030	(111)	Yes	45 × 45
3	37.441	(220)	No	45 × 45
4	50.000	(220)	No	45 × 45

and therefore additional scans at moderate ω values are required to centre the sample along the beam.

In an effort to evaluate the effectiveness of the method over an extended period of repeated use, Table 2 shows a record of Centre y positions, together with D as determined from the fit of the calibration images. The calibration images were taken over a period of six days, during which the beamline configuration (detailed in Table 3) and/or calibration sample were periodically changed. This is an appropriate practical measure of the method as the refined sample-to-detector distances obtained from calibration images are often the only reliable measure of D available to the user during a typical experimental run. While the data in Table 2 are not extensive, a number of interesting features are observed. Starting with the first seven entries, the Centre y values have a range of 20 µm, whereas D has a range of over 100 µm. The ranges for Centre y and D drop to 8 µm and 20 µm, respectively, if one considers the LaB$_6$ data from configuration 2 only. The Centre x values (not shown) have a range of almost 150 µm. Similarly, this range decreases to 84 µm if one considers the LaB$_6$ data from configuration 2 only. The large range of Centre x values, approximately one order of magnitude greater than that observed for Centre y, is consistent with the order-of-magnitude difference between the calculated corrections of Centre x and Centre y for $\Delta\omega = \pm 10°$, as shown in Fig. 4.

Turning now to the last four rows of Table 2, each pair of images was recorded without disturbing the sample position between images. Therefore the refined D values should ideally be the same for each respective pair. While the values are not the same, the differences of 9 µm and 21 µm for the first and second pair, respectively, are relatively small.

Finally, considering all of the entries together, it appears that the primary obstacle to establishing an accurate and consistent D is the number of counts recorded by the detector. For example, by switching to a larger collimator (configuration 1 → configuration 2), the flux at the sample was increased by almost an order of magnitude. This had little effect (5 µm) on

the calculated Centre y stage position, but had a significant effect (43 µm) on D. D was quite stable (a total range of 21 µm) in configuration 2 until the standard was changed to silicon. The higher symmetry and lower Z-value of Si as compared with LaB$_6$ result in fewer peaks and relatively fewer counts (for a given range of 2θ) used to refine the sample-to-detector distance. The discrepancy of over 100 µm for images taken with Si as compared with LaB$_6$ in configuration 2 is quite significant (note that a comparison of the Centre x and Centre y is not applicable, as the LaB$_6$ and Si calibration samples have separate mounts). Dera & Katrusiak (1999) report similar challenges, namely that source size and characteristics, as well as sample type, can have a significant influence on the results of the centring procedure described for single-crystal samples.

3.6. Centring summary

The centring method presented allows DAC samples to be positioned at an absolute unique position in space. The primary goal of the centring routine is to establish a consistent repeatable sample-to-detector distance D, and for LaB$_6$ data from beamline configuration 2, for which the most data were available, the refined values for D had a range of just over 20 µm, consistent with the variation observed when the sample was not disturbed between images. The method is valuable because it does not require a 180° rotation of the sample, which is often not feasible owing to the location of ancillary equipment present in high-pressure experimental configurations. Positioning the sample at the centre of rotation is a prerequisite for single-crystal studies, and it allows powder samples to be rocked during exposure. Because the characteristic transmission profile is due to the transmission contrast of the gasket and sample rather than the sample type itself, the method works equally well for powder and single-crystal samples. It is clear that the ultimate accuracy of the method depends on the ability to consistently identify a unique sample feature for all pertinent DAC rotation angles. This depends on a number of related factors including the anvils–gasket–sample region, as well as the actual scan parameters, all of which must be carefully considered in order to obtain the best possible result. However, it has been shown that, ultimately, the problem of defining a unique sample-to-detector distance is likely limited by the variance introduced by different calibration materials and/or beamline configurations.

4. Rocking

4.1. Overview

As discussed in the *Introduction*, the limited sample volume necessary to reach high-pressure conditions in the DAC, together with the near-parallel beam characteristic of typical synchrotron radiation sources, puts severe limits on the number of crystallographic planes satisfying the Bragg condition in polycrystalline samples. Consequently, poor counting statistics make it quite difficult to obtain reliable reproducible relative intensities. This difficulty is alleviated in part by the use of a flat two-dimensional detector such as those incorporating an imaging plate (IP) or charge-coupled device (CCD). By capturing entire Debye rings, the total intensity along a given ring can be summed, yielding a much more reliable intensity per unit length (of a given Debye ring) as compared with detection methods that record intensity from only a small portion of a given ring (as is often the case in conventional experimental configurations).

Area detectors, however, offer the added benefit of imaging, and, for the typical case when the DAC remains stationary during exposure, the images obtained frequently reveal spotty Debye rings as evidence of poor powder averaging. Qualitative accounts in the literature make it clear that rocking the DAC over a small angular range during image capture can significantly improve the homogeneity of intensity distribution along Debye rings (see, for example, Sakata *et al.*, 2004). However, the quantitative study presented here reveals that the benefits obtained by rocking are more substantial and varied than previously suggested. Interestingly, the results can be characterized by two distinct yet complimentary perspectives: improving intensity distribution and reducing detector saturation. Rocking the sample significantly increases the number of distinct crystallite orientations contributing to the total diffracted intensity, so, as one might expect, it improves the homogeneity of intensity distribution around Debye rings. But rocking also reduces the amount of time any particular group of crystallite orientations contributes to the total diffracted intensity, bringing about the less obvious result that it significantly reduces instances of detector saturation due to diffraction from large grains.

The latter perspective is of particular importance. IPs (and to a lesser extent CCDs) have a high dynamic range but, nevertheless, at the majority of second- and third-generation sources, exposure time is limited by detector saturation. Saturation results in lost information, such that an image with even a modest number of saturated pixels can no longer be relied upon for correct relative intensities. The obvious solution is to limit the exposure time, but this constitutes a compromise in achieving the best counting statistics. Sample rocking decreases the number of saturated pixels, thereby increasing the maximum exposure time; one makes the most of the detector's dynamic range for each image. Following some preliminary considerations associated with rocking, data are presented for various rocking scenarios, at both ambient and high-pressure conditions. The results are accompanied by a detailed discussion in the contexts of the two distinct yet
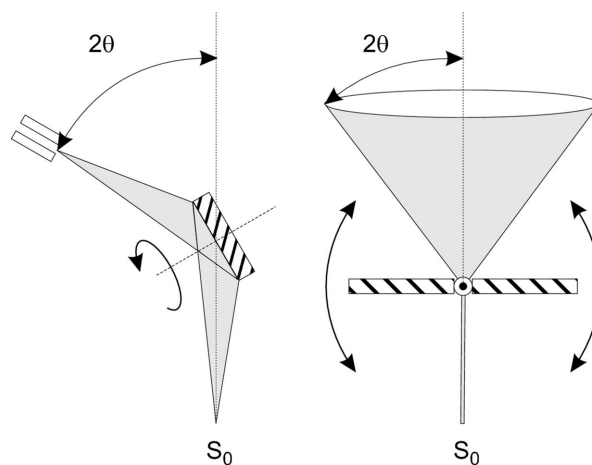
complimentary perspectives of improving intensity distribution and reducing detector saturation.

4.2. Rocking *versus* spinning

At the outset it is worth briefly clarifying what is meant by sample rocking, and distinguishing it from similar strategies such as sample spinning, a technique often employed in conventional θ–2θ diffraction geometries. Fig. 5 offers a schematic view of the situation. In the case of a conventional θ–2θ reflection geometry (Fig. 5, left), only grains with sets of planes {*hkl*} parallel to the sample holder contribute to the diffracted intensity as recorded by the detector. By spinning the sample holder about its normal axis, these planes remain essentially parallel to the sample holder. In short, spinning does little to change the orientation of these planes with respect to the beam; instead it may bring new grains into the path of the beam, increasing the number of grains which contribute to the observed intensity at a particular angle 2θ.

The situation is quite different in the case of transmission geometry using an area detector (Fig. 5, right). Data are collected simultaneously over the entire relevant 2θ range, such that all crystallites with planes satisfying the Bragg condition for the relevant 2θ range contribute to the observed intensity. Sample rocking involves rotating the DAC over a modest angular range about an axis normal to the incident beam. The result is that all of the grains contained in the irradiated sample volume will have a new orientation with respect to the incident beam. In short, rocking is far more effective than spinning in the context of changing the orientation of pertinent grains. This is imperative as the limited sample volume of the DAC does not afford the luxury of bringing a significant number of new grains into the path of the incident beam.

The rocking method employed in this work does not involve a continuous sweeping motion of the sample through the specified angular range, but rather the sample is rotated by

Figure 5
Schematic diagrams comparing the practice of sample spinning (left), often employed in conventional laboratory diffractometers, with the practice of sample rocking (right), employed in the present work. S_0 indicates the location of the X-ray source.

discrete intervals dictated by the user. Specifically, rocking is carried out by a simple macro which requires the user to input the end points of the rocking range, the discrete step size and the total exposure time. This information is used, together with the dynamic parameters of the rotation stage, to rock the sample over the entire range once during the specified exposure time, with the appropriate discrete step size. Note that rocking ranges as discussed in this work are complete and symmetric; a rocking range of 8° corresponds to rocking the DAC $\pm 4°$ about the rotation axis origin.

4.3. Image series

The majority of the data were taken using a powder sample of LaB_6 (National Institute of Standards and Technology, Standard Reference Material 660a) under ambient conditions. To mimic the sample volume typically encountered in a DAC, the calibration standard was loaded into an indented gasket, as described above in the centring portion of this work. Depending on a number of factors including the type and/or quality of sample and type (or lack) of pressure-transmitting medium, application of pressure can introduce a number of complications including, for example, anisotropic strain broadening and/or preferred orientation. This makes a comprehensive quantitative evaluation of sample rocking at high pressure difficult. Therefore an almost ideal powder was chosen for the greater part of the study, with images taken at ambient pressure. However, an example of rocking at high pressure will also be presented below. Regarding the use of an IP area detector, despite the widespread use of CCDs at synchrotron radiation facilities, the combination of high dynamic range, exceptionally large area and tolerable readout time has resulted in IPs continuing to be the workhorses for most high-pressure powder X-ray diffraction studies. However, the characteristics of current CCDs are such that the issues of saturation and pixel bleeding are of key importance. The results presented here should be generally applicable to CCDs as well.

Three image series, each consisting of six powder X-ray diffraction images, were collected. For each of the first two series, a reference image was taken without rocking and with intentional overexposure to ensure a modest number of saturated pixels would be observed. Subsequent images were then taken with sample rocking, starting with a nominal rocking range and then doubling it for each subsequent image, all with a constant step size of 0.1°. For the third image series, a constant rocking range of 8° was used while the initial step size of 0.8° was halved for each subsequent image. Table 4 summarizes these key parameters for each series. In each series, care was taken to expose each image to the same incident photon intensity as determined by the number of total ion chamber counts.

4.4. Results and analysis

4.4.1. Improving intensity distribution. To appreciate the difference rocking can make in the context of improving intensity distribution, it is most instructive to examine the
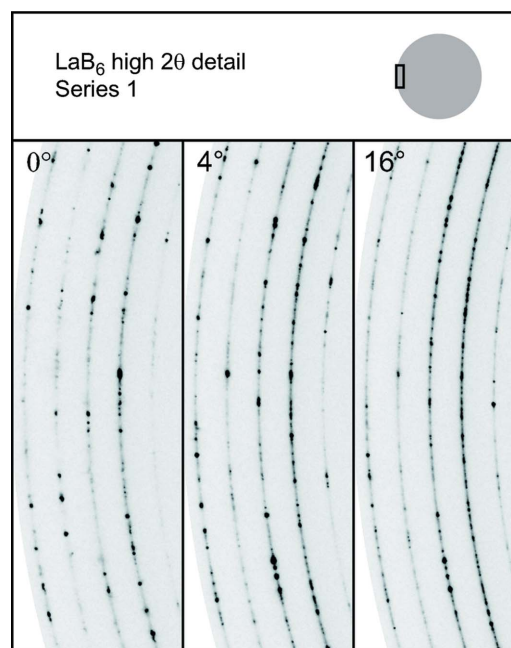
Table 4
Beam dimensions, rocking range and discrete step size for each of the three image series.

Series	Beam size (μm)	Rocking range (°)		Step size (°)	
1	15 × 15	Variable	0–16	Fixed	0.1
2	45 × 45	Variable	0–32	Fixed	0.1
3	45 × 45	Fixed	8	Variable	0.8–0.025

Debye rings observed at the highest 2θ values. There are several reasons why this is the case, but let it suffice to point out that these Debye rings are the least intense, and this weak intensity is distributed along the rings of greatest circumference. Fig. 6 shows a small region of the detector for three separate images from series 1. The salient feature of series 1 is the small incident beam size, resulting in a minute irradiated sample volume ($\sim 10^{-8}$ cm³), making it particularly difficult to obtain an even azimuthal intensity distribution. This is particularly noticeable in the case of the stationary DAC (Fig. 6, left), where the rings can be described, for the most part, as intermittent spots superimposed on extremely faint rings. At the maximum rocking range of the series (Fig. 6, right), the rings appear much more homogeneous; the spotting is less prevalent and the continuous rings appear more intense.

To explore this improvement quantitatively, the observed intensity of the (331) reflection was rebinned as a function of azimuthal angle (*i.e.* along the Debye ring) for images in all three series. The (331) reflection was chosen because it was the largest Debye ring, at approximately 31.4° 2θ, captured in its

Figure 6
High 2θ detail of the detector (indicated by the small rectangle, with respect to the full image area, in the figure heading) for selected images from series 1. Note that as the rocking range (indicated in the upper left corner of each image) increases from the stationary sample (left) to the maximum rocking range of the series (right), the Debye rings exhibit a marked improvement in homogeneity of intensity distribution.

Table 5
Basic statistical information for the (331) reflection collected from 1400 azimuthal bins (from 5° to 355° by 0.25°) of fixed width ($2\theta \simeq 0.5°$).

In general, the mean intensity increases only slightly with rocking, suggesting that area detectors are quite effective in yielding reliable relative intensities, even for stationary samples. In general, the standard deviation about the mean and the total intensity range decreases significantly with rocking, suggesting that rocking is crucial to obtaining a more homogeneous distribution of intensities, with fewer occurrences of extreme (saturated) intensity.

Series	Range (°)	Step size (°)	Mean (counts)	Standard deviation (counts)	Intensity range (counts)
1	0	0.1	187	124	2869
	1		192	113	2501
	2		195	86	1332
	4		197	116	3037
	8		196	71	1567
	16		195	51	814
2	0	0.1	663	407	7656
	2		709	288	3187
	4		729	317	4055
	8		714	217	2220
	16		711	162	1792
	32		729	135	1473
3	8	0.8	651	254	3601
		0.4	683	217	2483
		0.2	664	194	1839
		0.1	695	211	2031
		0.05	672	204	2013
		0.025	663	200	1945

entirety by the detector. Specifically, the intensity recorded in a 3 mm strip (spanning approximately 0.5° 2θ) straddling the Debye ring was rebinned every quarter of an azimuthal degree, resulting in a total of 1440 bins. Table 5 shows the results of a basic statistical analysis carried out on the rebinned data. (Note that only a total of 1400 data points were considered in the analysis inasmuch as a 10-azimuthal-degree region was omitted to ensure the portion of the detector shielded by the beam stop did not contribute to the statistics.)
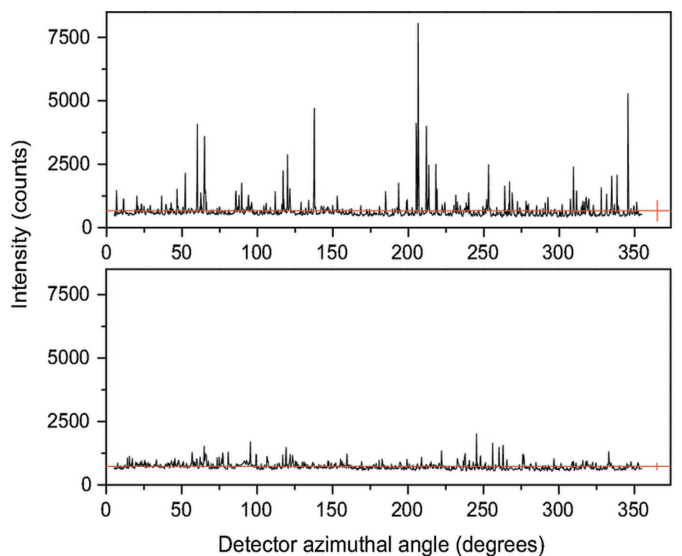
Some general (although not exclusively monotonic) trends arise in all three series as the rocking range is increased or as the step size is decreased: the mean intensity increases, while at the same time the standard deviation about the mean and the total range of observed intensities decrease. The combination of these three factors clearly demonstrates that the distribution of intensities along the (331) Debye ring is more homogeneous with rocking. (Note that a statistical analysis was carried out for three other rings in each image, with corroborating results; however, the details have been omitted for the sake of brevity.)

Looking a little more closely at the mean intensities in the first two series, the difference between the stationary DAC and the smallest rocking range is perhaps appreciable, but a subsequent increase in the rocking range does not result in a significant increase in the mean intensity. This is not surprising inasmuch as care was taken to expose the sample to the same number of counts for each image. Conversely, the decrease (*i.e.* the improvement) in the standard deviation is substantial as the rocking range is increased. This can readily be explained
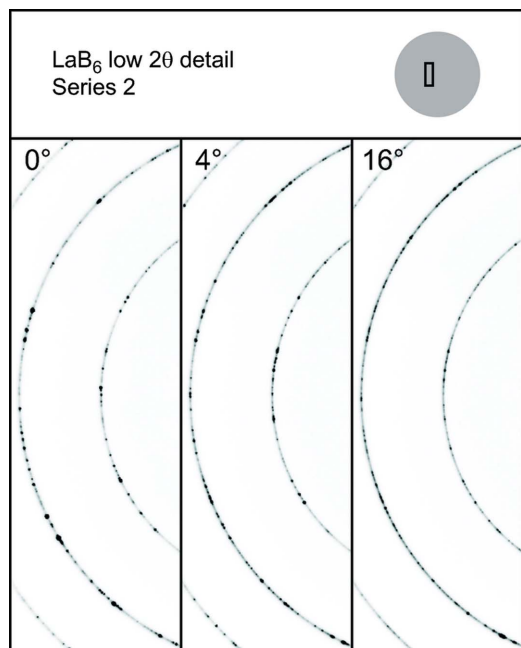
by an increase in the number of distinct crystallite orientations during exposure. The combination of these two factors leads to the conclusion that, although rocking improves the distribution of the intensities, it does not significantly affect the total observed intensity. In short, area detectors are quite effective in yielding reliable relative intensities, even in the absence of rocking (at least in the case of a good powder under ambient conditions).

To appreciate the difference in the total range of observed intensities, Fig. 7 provides a comparison of the intensity *versus* azimuthal angle for the (331) reflection in the case of the stationary DAC (top) as well as rocking over 32° (bottom) for images from series 2. The difference between the two is immediately apparent, further demonstrating that the intensity along the rings is more evenly distributed when the DAC is rocked. It should be reiterated that, despite the intense spikes observed in the case of the stationary DAC, the mean intensity is less than that observed for any of the rocking ranges. The significant reduction in the total range of observed intensities can be looked at not only from the perspective of improving intensity distribution but also from the perspective of reducing detector saturation. This latter perspective is further developed in the following section.

4.4.2. Reducing detector saturation. To appreciate the difference rocking can make in the context of reducing detector saturation, it is most instructive to look at the Debye rings at low 2θ values. Not only are these the most intense rings, but this strong intensity is packed into rings with the shortest circumference. It is these rings which will saturate first in the event of overexposure. The importance of this point cannot be overstressed; when it comes to data analysis (*e.g.* structural refinement), strong reflections can carry significant weight in a number of respects, including line shape and lattice

Figure 7
Intensity *versus* azimuthal angle for the (331) reflection for the stationary sample (top) and for the maximum rocking range of 32° (bottom) from series 2. Note that both are plotted on the same intensity scale to contrast the marked influence that sample rocking has on intensity distribution. The horizontal lines indicate the mean intensity and the vertical bars at the right indicate the standard deviation of the respective plots.
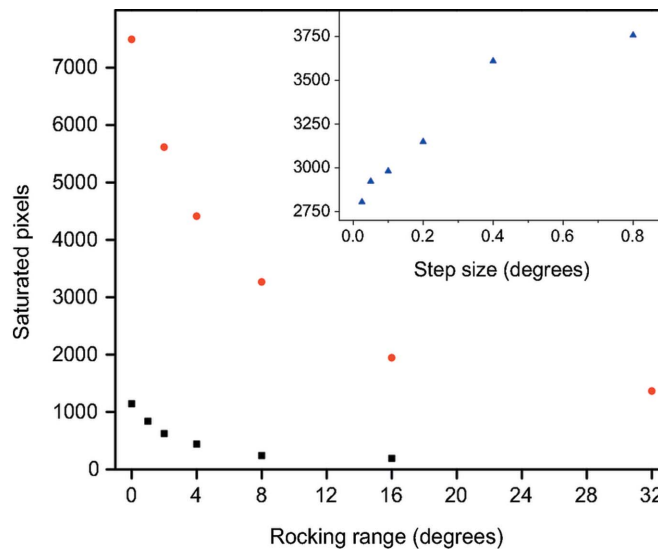
Figure 8
Low 2θ detail of the detector for selected images from series 2. Note that as the rocking range increases from the stationary sample (left) to a rocking range of 16° (right), the Debye rings exhibit a marked decrease in the occurrence of intense Bragg spots superimposed on the Debye rings.
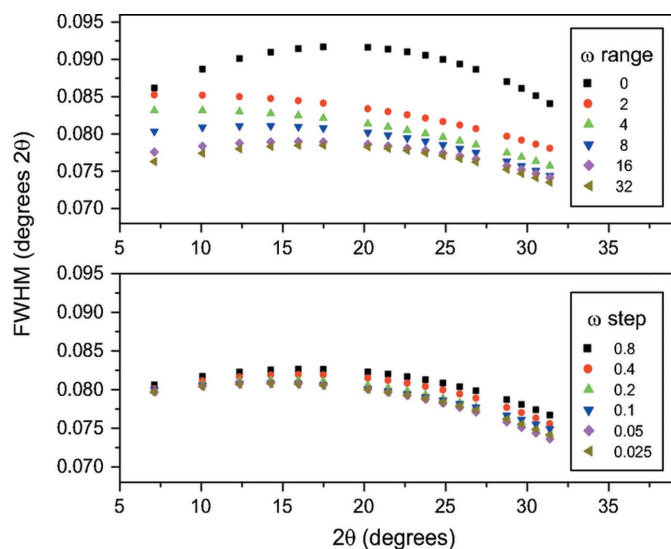

Figure 9
Number of saturated pixels *versus* rocking range for series 1 (squares) and series 2 (circles). At the maximum rocking range, for both series the number decreases by more than 80% as compared with the stationary sample. The inset is a plot of the number of saturated pixels *versus* step size for series 3 (triangles), showing a more modest decrease of approximately 25%.

constants. Also, relative intensities are often defined in terms of the most intense peak. Unfortunately, it is the most intense peaks which are most susceptible to intensity inaccuracies owing to pixel saturation.

Fig. 8 shows a portion of three images from series 2. In the case of the stationary DAC (Fig. 8, left), the reflections are marked by intense Bragg spots superimposed on Debye rings. As the DAC is rocked (Fig. 8, centre) and as the rocking range is subsequently increased (Fig. 8, right), the occurrence of the intense Bragg spots is significantly reduced, resulting in a more consistent line width along the rings. Also, the expected improvement in intensity distribution is noticeable.

Turning to a quantitative evaluation of the benefits, Fig. 9 shows the number of saturated pixels ($I_{pixel} > 65535$ counts for the mar345 detector at 100 µm pixel resolution) as a function of the rocking range for series 1 and 2. In each series the number of saturated pixels fell by over 80% at the maximum rocking range (16° and 32° for series 1 and series 2, respectively) as compared with the stationary DAC. The inset of Fig. 9 shows the number of saturated pixels as a function of step size for the constant rocking range of 8°. Interestingly, for the smallest step size, the decrease in saturated pixels is only 25% as compared with the largest step size. In this particular case it is clear that both increasing the rocking range and decreasing the step size are effective in minimizing detector saturation; however, the maximum potential is primarily dependent on the overall rocking range, as this ultimately determines the maximum number of unique crystallite orientations that contribute to the intensity observed in the diffraction image.

4.4.3. Rietveld analysis. Full-pattern structural refinements were carried out on all of the diffraction patterns from the three image series. One cannot overstate the importance of starting out with the highest quality data possible when carrying out such refinements. In the present work, however, poor data were intentionally collected in an effort to accentuate the effect that rocking has on reducing detector saturation; the reader should bear this in mind when considering the absolute results of the refinements. Notwithstanding this, some interesting results emerge from the analyses, which further demonstrate some of the benefits obtained by rocking polycrystalline samples.

The intense Bragg spots result in small bulges of intensity around the Debye rings. As these are progressively removed through rocking, the line width of the rings should progressively decrease. Fig. 10 (top) shows the line width *versus* 2θ for series 2. The most striking difference is observed between the stationary DAC and the 2° rocking range. In the case of the stationary DAC, the intense Bragg spots significantly affect the line width and, as the scattering angle is increased, this impact is exacerbated as the projections of intense Bragg spots onto the flat area detector increase by a factor of $\sim 1/\cos(2\theta)$, resulting in a maximum line width observed at $2\theta \simeq 18°$. At still higher 2θ, saturation effects are less prominent and the line width decreases accordingly. With even the most modest rocking range of 2°, the effects of pixel saturation are mitigated such that the line width remains roughly constant up to $2\theta \simeq 18°$, after which it decreases in a manner similar to that observed with the stationary DAC. Subsequent increases in rocking range show a systematic (although less pronounced) decrease in line width. Furthermore, the change in the overall shape of the curves is minimal, suggesting that rocking over

Figure 10
Line width *versus* 2θ for series 2 (top) and series 3 (bottom). Sample rocking decreases line width by minimizing the occurrence of intense Bragg spots, pixel saturation and pixel bleeding.

Table 6
Quality of fit and overall displacement factors from Rietveld refinements of diffraction patterns from series 1 and 2.

Note that by reducing the number of saturated pixels recorded for low 2θ peaks the displacement parameter B goes from negative to positive.

Series	Rocking range (°)	R_{wp} (%)	R_{Bragg} (%)	$B_{overall}$ (Å²)
1	0	4.20	2.60	−0.13 (3)
	1	4.01	2.35	−0.17 (2)
	2	3.73	2.23	−0.12 (2)
	4	4.24	2.59	−0.12 (2)
	8	3.73	2.19	0.05 (2)
	16	3.69	1.70	0.19 (2)
2	0	4.64	2.53	−0.42 (2)
	2	4.86	3.14	−0.37 (2)
	4	4.55	2.82	−0.30 (1)
	8	4.70	2.57	0.94 (2)
	16	4.58	2.51	1.12 (2)
	32	4.46	2.13	0.99 (2)

even a small range results in a more appropriate line shape. Notably, at the highest 2θ values, the line width remains roughly constant for ranges greater than $8°$, suggesting that the effects of pixel saturation are essentially eliminated for these reflections. Fig. 10 (bottom) shows the line width for series 3. Note that the observed line width is almost exactly that observed for the $8°$ range from series 2, as expected. The decrease in line width is measurable, yet minimal as compared with series 1 and 2 (much like the decrease in saturated pixels). Again, it is clear that both range and step size play a role in minimizing line width, but range appears to play the dominant role.

Mixed results were obtained for the quality of the fits. Table 6 shows the R-factors for the images of each series. Series 1 exhibited a general trend of decreasing R values with increased rocking range; however, this was not the case for series 2. The refined parameters included an overall isotropic displacement (sometimes referred to as a temperature) factor. The refined values for B, shown in the final column in Table 6, reveal an important benefit of rocking (or more appropriately, minimizing saturated pixels). To clarify, the B parameter accounts for the mean-square displacement of the atoms from their equilibrium position, and if the magnitude of this displacement is appreciable with respect to the distance between a particular set of planes $\{hkl\}$ an appreciable decrease in observed diffraction intensity will result. By definition, B is positive. However, in the least-squares refinement procedure employed by *FullProf* there is no restriction on the sign of B (except that it is explicitly constrained by the user prior to refinement), and a physically meaningless negative B value can be obtained if the observed intensity for high 2θ reflections is too large relative to the intensity for low 2θ reflections. As stated earlier, saturated pixels were masked prior to data analysis, such that they did not contribute to the measured intensities of the resulting diffraction patterns.
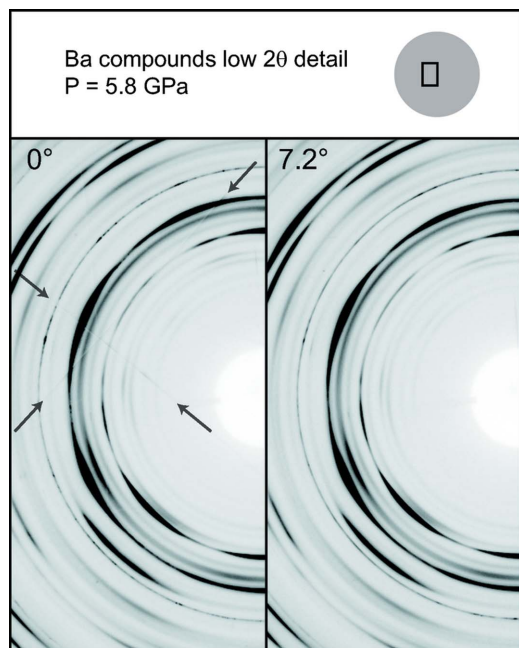
Therefore the intensities of low 2θ reflections (where the majority of saturated pixels occurred) are too low relative to the higher 2θ reflections, resulting in a negative B value. As the rocking range was increased, the intensity information lost to masked pixels decreased, and eventually the detector saturation was reduced to the point that positive B values were obtained. For brevity, the detailed results for series 3 have been omitted from the table as there was less variation with the constant rocking range; however, the average value of the results were $R_{wp} = 4.68\%$, $R_{Bragg} = 2.34\%$ and $B = 0.72$ Å², similar to the results obtained from the series 2 image rocked over $8°$.

4.5. Application of pressure

Applying pressure to a sample introduces additional challenges which make it difficult to immediately appreciate the benefits of rocking. However, rocking is essential to improving the quality of data recorded from less-than-ideal samples. Depending on the particular sample, as well as the type (or lack) of pressure-transmitting medium used, X-ray diffraction images exhibit a number of features that may not be apparent at atmospheric pressure. Line width can be significantly broadened not only by intense Bragg spots but also by small crystallite size or by anisotropic strain in crystallites. The intensity distribution along Debye rings can vary significantly not only because of limited sample volume but also because of preferred orientation of crystallites owing to crystal growth habit and/or non-hydrostatic conditions.

Fig. 11 shows portions of two images from a sample containing a mixture of barium compounds (Smith *et al.*, 2007) at approximately 5.8 GPa (no pressure-transmitting medium was used as BaH_2 is extremely hygroscopic). At a glance, it is not apparent that the intensity distribution has been significantly improved by rocking, nor is it apparent that there are fewer intense regions. In fact, the striking feature is that the two images are almost identical in appearance. However, even in this severe case of crystallite strain and texture, rocking still
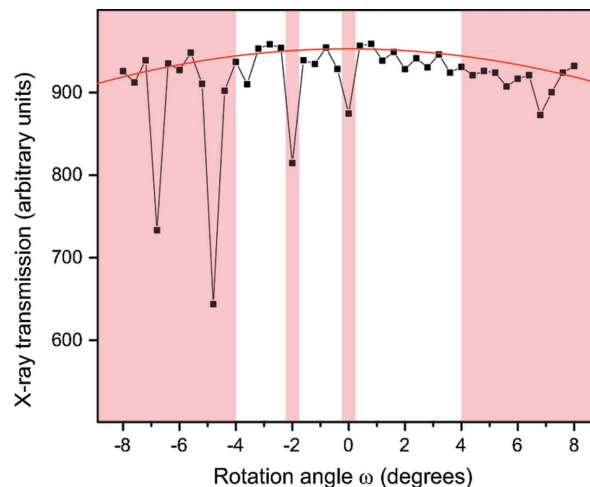
Figure 11
Low 2θ detail of the detector for selected images from experiments on barium compounds at high pressure. A visual comparison of the two images shows few differences; however, there is a respectable decrease, approximately 20%, in the number of saturated pixels in the case of the rocked DAC. Additionally, Kossel lines arising from the diamond anvils in the stationary DAC image (indicated by the arrows) are no longer present when the DAC is rocked.

has a measurable effect. Rocking the DAC resulted in a decrease in the number of saturated pixels by 20% as compared with that observed for the stationary DAC. This is not as significant as the over 50% decrease observed for LaB_6 when rocked by 8°, but it is important to note that in the case of the standard the saturated pixels are due to discrete intense Bragg spots, whereas in the case of the barium compounds saturation is caused by preferred orientation resulting in significant portions (at periodic azimuthal angles) of the low 2θ rings reaching saturation level.

An additional, albeit minor, benefit brought about by rocking the DAC is that the Kossel lines (faintly visible in the reproduction of Fig. 11, left, but clearly visible in the original image) recorded with the stationary DAC disappear with rocking. Kossel lines arise from the edges of the diamond anvil facets. While these lines rarely cause any difficulty, they can occasionally influence observed intensities if by chance they coincide with a significant portion of a Debye ring (see, for example, Moriwaki *et al.*, 2006). Rocking the sample in turn rocks the diamond anvils, which removes any visible Kossel lines.

Interestingly, in the case of rocking, approximately 10% of the saturated pixels are due to diamond Bragg spots which were not observed in the case of the stationary DAC. Adding the anvils constitutes adding two very large single crystals to the experimental configuration, and as the sample is rocked the diamonds will invariably satisfy the Bragg condition at

Figure 12
X-ray transmission through the DAC as a function of rotation angle ω. The measured values (squares) are connected with lines to emphasize dramatic dips in intensity owing to diffraction from the diamond anvils. The solid arc near the top of the plot indicates the approximate intensity fall-off expected owing to the increase in path length through the diamonds as the DAC is rotated. The shaded portions detail the rocking range for Fig. 7: the shaded portions on the far left and right indicate the limits of the rocking range, whereas the two narrow shaded portions indicate regions omitted from the total rocking range.

certain rocking angles. Consequently, the diffracted intensity recorded by the detector can be significant.

Fig. 12 shows a plot of the X-ray transmission through the DAC as a function of ω. The arc across the top of the plot is an estimate of the expected transmission owing to the effective change in thickness of the diamond as a function of ω. There are several moderate and a few severe intensity dips below this line owing to diffraction from the diamonds, which removes a number of photons from the transmitted beam *via* primary extinction. Of course, it is not necessarily the case that all of the Bragg spots indicated by the dips will fall on the detector, but invariably some of them do, and the intense spots reach saturation extremely quickly as compared with instances of saturation coming from the sample. One strategy is to avoid the angular ranges coinciding with the most intense diamond diffraction. In the macro used in the experimental control software, an option was incorporated to omit discrete angular ranges within the overall rocking limits. The shaded regions in Fig. 12 denote angular ranges omitted when rocking the DAC. In fact, Fig. 12 was obtained from the sample containing the barium compounds, so if the reader notes that the high-pressure sample in Fig. 11 was rocked over a range of 7.2°, it was actually rocked over 8° (−4° to 4°), omitting two regions totalling 0.8°. It should be noted that the rotation velocity of the stage is such that an omitted region is skipped in less than a second. This is sufficient to avoid significant diffraction at moderate X-ray sources. For intense sources where images are captured in a few seconds as opposed to a few minutes (see, for example, Mezouar *et al.*, 2005), it might prove necessary to use a high-speed shutter to block the beam during rotation through omitted ranges.

4.6. Rocking summary

From the preceding data it is clear that rocking significantly improves the quality of high-pressure powder diffraction images in two complimentary ways. First, it promotes a more homogeneous intensity distribution along Debye rings, and second, it reduces the occurrence of detector saturation. Regarding intensity distribution, for good powders which do not suffer too severely from strain or texture, the improvement is obvious. In the case of difficult samples, it is not clear that rocking will significantly improve the intensity distribution. An interesting result is that the data reinforce the idea that the use of an area detector to capture complete Debye rings is quite effective in yielding good intensities, even in the case of the stationary DAC.

The area detectors most commonly employed in high-pressure powder X-ray diffraction studies have a high, but nevertheless limited, dynamic range. The reduction of detector saturation was substantial for both the Standard Reference Material as well as the high-pressure sample, the latter suffering from a number of complicating factors. It is this aspect of sample rocking that is arguably most crucial. In practice, the number of saturated pixels should be minimal, and typically, exposure time is reduced to achieve this. However, rocking will allow exposure time to be increased slightly, in the end allowing one to make better use of the detector's full dynamic range. Furthermore, by reducing intense Bragg spots, other benefits such as decreased line width were observed. DAC samples should be rocked over the largest possible range with the smallest possible step size to maximize the number of unique crystallite orientations with respect to the beam and minimize the amount of time that any particular orientation contributes to the diffracted intensity.

5. Conclusion

The selected techniques described above can play a crucial role in optimizing the quality of data obtained when carrying out diamond anvil cell crystallography. Accurate reproducible positioning of samples at a unique position in the experimental configuration is critical as it allows the sample-to-detector distance obtained from images of calibration standards to be correctly applied to data analysis of research samples. The centring technique described above provides excellent results, while at the same time offering the flexibility often required to accommodate various (and often crowded) experimental configurations commonly encountered at synchrotron radiation facilities. Properly locating the sample at the centre of rotation affords the possibility of rocking polycrystalline samples during X-ray exposure. This practice is of particular importance to high-pressure diamond anvil cell crystallography, as the sample volume is severely limited. Rocking clearly yields the expected effect of improving the distribution of intensity along Debye rings. More importantly, it limits detector saturation by limiting the amount of time large grains assume a particular orientation with respect to the incident X-ray beam. These techniques are conceptually quite simple, and with a modicum of care exercised by the user they can be used to great effect; they should be incorporated as routine practices when carrying out diamond anvil cell crystallography.

References

Budzianowski, A. & Katrusiak, A. (2004). *High-Pressure Crystallography*, edited by A. Katrusiak and P. McMillan, pp. 101–112. The Netherlands: Kluwer.

Dera, P. & Katrusiak, A. (1999). *J. Appl. Cryst.* **32**, 510–515.

Hamilton, W. C. (1974). *International Tables for X-ray Crystallography*, Vol. IV, pp. 273–284. Birmangham: Kynoch Press. (Present distributor Kluwer Academic Publishers, Dordrecht.)

Hammersley, A. P., Svensson, S. O., Hanfland, M., Fitch, A. N. & Häusermann, D. (1996). *High Pres. Res.* **14**, 235–248.

King, H. E. & Finger, L. W. (1979). *J. Appl. Cryst.* **12**, 374–378.

Kunz, M., MacDowell, A. A., Caldwell, W. A., Cambie, D., Celestre, R. S., Domning, E. E., Duarte, R. M., Gleason, A. E., Glossinger, J. M., Kelez, N., Plate, D. W., Yu, T., Zaug, J. M., Padmore, H. A., Jeanloz, R., Alivisatos, A. P. & Clark, S. M. (2005). *J. Synchrotron Rad.* **12**, 650–658.

Mezouar, M., Crichton, W. A., Bauchau, S., Thurel, F., Witsch, H., Torrecillas, F., Blattmann, G., Marion, P., Dabin, Y., Chavanne, J., Hignette, O., Morawe, C. & Borel, C. (2005). *J. Synchrotron Rad.* **12**, 659–664.

Moriwaki, T., Akahama, Y., Kawamura, H., Nakano, S. & Takemura, K. (2006). *J. Phys. Soc. Jpn*, **75**, 074603.

Rodriguez-Carvajal, J. (2006). *FULLPROF*, version 3.70, July 2006. ILL, Grenoble, France.

Ruoff, A. L., Luo, H., Vanderborgh, C., Xia, H., Brister, K. & Arnold, V. (1993). *Rev. Sci. Instrum.* **64**, 3462–3466.

Sakata, M., Itsubo, T., Nishibori, E., Moritomo, Y., Kojima, N., Ohishi, Y. & Takata, M. (2004). *J. Phys. Chem. Solids*, **65**, 1973–1976.

Smith, J. S., Desgreniers, S., Tse, J. S. & Klug, D. D. (2007). *J. Appl. Phys.* **102**, 043520.